

## **Computational techniques for the analysis and design of dielectric-loaded plasmonic circuitry**

**Odysseas Tsilipakos · Alexandros Pitilakis ·  
Anna C. Tasolamprou · Traianos V. Yioultsis ·  
Emmanouil E. Kriezis**

Received: date / Accepted: date

**Abstract** The finite element and the beam propagation method, two widely used methods in photonics, are utilized for the analysis of plasmonic components based on the dielectric-loaded plasmonic waveguide. Two components are chosen as examples and are subsequently numerically investigated by employing the aforementioned methods, in order to demonstrate their applicability in plasmonics. Specifically, a microring resonator add-drop filter and a Mach-Zehnder interferometric switch are analyzed by means of the finite element and the beam propagation method, respectively. The formulation adopted is clearly presented in both cases and the case-dependent implementation details are thoroughly discussed.

**Keywords** Dielectric-loaded plasmonic waveguide · Plasmonic components · Thermo-optic effect · Finite element method · Beam propagation method

**PACS** 42.82.-m · 42.82.Et · 73.20.Mf · 71.36.+c

### **1 Introduction**

The field of guided-wave plasmonics, a research area concerned with the manipulation and routing of surface plasmon polaritons (SPPs), has attracted considerable attention in recent years. SPPs are electromagnetic surface waves coherently coupled to collective oscillations of a metal's free electron density (Raether 1988). They propagate along a metal-dielectric interface and feature an exponential decay of the field components away from it. Plasmonic waveguides comprising at least one metal-dielectric interface can support guided modes having a lateral spatial extent (spot size) of sub-wavelength dimensions. As a result, plasmonic components can be employed in nanophotonic integrated circuits, combining the bandwidth of photonics along with nanoscale dimensions (Ebbesen et al 2008; Gramotnev and Bozhevolnyi 2010).

O. Tsilipakos · A. Pitilakis · A. C. Tasolamprou · T. V. Yioultsis · E. E. Kriezis  
Department of Electrical and Computer Engineering, Aristotle University of Thessaloniki, Thessaloniki GR-54125, Greece  
Tel.: +30-2310-996362, Fax: +30-2310-996312  
E-mail: otsilipa@auth.gr

During the last few years, several types of plasmonic waveguides have been proposed, in pursuit of a tightly confining structure, suitable for densely integrated plasmonic circuits, which would moreover feature tolerable propagation losses. Each of them has been employed in the implementation of a broad range of passive components including waveguide bends, power splitters, Mach-Zehnder interferometers, and microring/disk resonator filters. Obviously, the numerical investigation of the performance characteristics of such components is essential, in order to identify optimal designs and subsequently realize efficient plasmonic circuits. So far, several numerical methods have been utilized for the task. These include the finite-difference time-domain (FDTD) method (Wu et al 2010), the finite-difference frequency-domain (FDFD) method (Yu et al 2008), and the finite element method (FEM) (Krasavin and Zayats 2008; Tsilipakos et al 2009; Tsilipakos and Kriegis 2010). Surprisingly, the Beam Propagation Method (BPM), a widely used method in other photonics technologies, has not yet received much attention in plasmonics. In section 3, we will show that it can be successfully applied to model light propagation in plasmonic components as well.

Among the recently proposed 2D plasmonic waveguides, i.e., able to confine light in both transverse directions, the dielectric-loaded plasmonic (DLSPP) waveguide offers some distinct advantages: It is technologically simple, consisting of a dielectric ridge residing on a metallic film, and exhibits strong guiding properties along with relatively low propagation losses ( $L_{\text{prop}} \sim 50 \mu\text{m}$  for the fundamental,  $\text{TM}_{00}$ , mode). Various DLSPP-based plasmonic components have been experimentally characterized and theoretically investigated, with wavelength-selective ones (Holmgard et al 2009a,b; Tsilipakos and Kriegis 2010) being of substantial interest, since they can provide the necessary functionalities needed to assemble fully operational plasmonic circuits. Another significant advantage of the DLSPP waveguide is that the loading material forming the ridge can be a thermo-optic polymer, therefore introducing a means of providing DLSPP-based components with tuning capabilities. By following this approach, thermally-tunable components have been demonstrated (Tsilipakos et al 2009; Gosciniak et al 2010).

In this work, we focus on the application of two numerical methods, namely the finite element and the beam propagation method, in the analysis of DLSPP-based plasmonic components. Each method is suited to a different class of components with distinct characteristics. Specifically, the FEM can handle up to medium-sized components exhibiting any kind of resonant or reflecting behavior, while the BPM can deal with much larger structures, provided that there is a clear axis of propagation and no reflections. In what follows, a typical component belonging to each class is chosen and numerically analyzed with the corresponding method, in order to demonstrate the applicability of the aforementioned methods in plasmonics. Specifically, the FEM is employed in the numerical investigation of a DLSPP-based microring resonator add-drop filter, while the BPM is utilized for the analysis of a DLSPP-based Mach-Zehnder interferometric (MZI) switch. The formulation adopted is clearly presented for both methods and any case-dependent implementation details are thoroughly discussed.

Throughout this paper, the DLSPP waveguide is made of a  $w \times h = 500 \times 600 \text{ nm}^2$  thermo-optic polymer ridge with a typical refractive index of 1.5 and a thermo-optic coefficient (TOC) of  $-2 \times 10^{-4} \text{ K}^{-1}$ , a value close to the ones of currently available materials. The dimensions of the polymer ridge ensure single-mode operation in the vicinity of the  $1.55 \mu\text{m}$  telecommunication wavelength (Holmgard and Bozhevolnyi 2007). The gold film is  $d = 100 \text{ nm}$  thick and for its refractive index a value of  $0.55 - j11.5$  is adopted (Palik 1985). For the purpose of thermal addressing, the metallic film is restricted into having a finite width. Width values smaller than  $3 \mu\text{m}$  result in a gradual decrease of the propagation

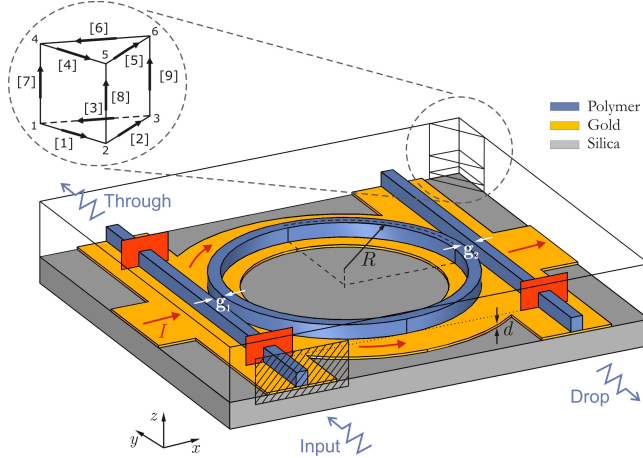


**Fig. 1** Schematic of a DLSPP-based microring add-drop filter. The input port at which the mode is fed is marked by a ruled rectangle. Fictitious power ports at which guided power is calculated are shown in red. The orientation of the triangular prism mesh as well as the element itself with node and edge numbering are also included. For illustration clarity only one prism per material layer is drawn—more are actually used.

length with respect to the reference case of infinite width (Grandidier et al 2010), and are, thus, avoided. Finally, the combined structure of polymer ridge and metallic film resides on a 1  $\mu\text{m}$ -thick silica substrate.

The paper is organized as follows: In section 2 the operating principle of the microring resonator add-drop filter is presented and the choice of the finite element method for its analysis justified. The following subsections, 2.1 and 2.2, introduce the implementation details of the finite element method and present the obtained results, respectively. Section 3 deals with the modeling of the Mach-Zehnder interferometer. The major formulation aspects and implementation details of the numerical method utilized, i.e., the BPM, are outlined in subsection 3.1. In subsection 3.2 the design procedure is discussed and the obtained results presented. Finally, section 4 provides the concluding remarks.

## 2 The finite element method for plasmonic components

As mentioned in the introduction, the FEM can readily handle structures of resonant nature such as the microring resonator add-drop filter: a wavelength-selective component consisting of a microring resonator coupled to two access waveguides (Fig. 1). Light entering the input waveguide is directed toward the two output ports (through and drop) with a power ratio which depends on the operating wavelength. Minima of the through port transmission, and consequently maxima of the drop port transmission, are observed for operating wavelengths satisfying the microring resonance condition. The vectorial three-dimensional finite element method (Jin 2002) is highly suited for the modeling of the aforementioned component for several reasons. Firstly, the boundary conforming mesh of the finite element method can accurately model the cylindrical shape of the resonator involved. Secondly, the boundary conditions at interfaces between different materials are inherently satisfied, and are not hindered by the dramatic discontinuities of the dielectric permittivity on polymer-gold interfaces, which would pose problems in finite-difference-based methods. Finally, the resonant nature of the component on one hand precludes certain methods like the BPM, which can

handle only forward-propagating waves, and on the other hand, renders time-domain methods time-consuming, since stepping must be carried on until all energy leaves the resonator.

## 2.1 Method implementation details

Triangular prism (edge) elements of the first order are used for the discretization of the vector wave equation:

$$\nabla \times \bar{\mu}_r^{-1} \nabla \times \mathbf{E} - k_0^2 \bar{\epsilon}_r \mathbf{E} = \mathbf{0}. \quad (1)$$

This choice of elements is justified by the planar nature of the structure and leads to a reduced number of degrees of freedom (DoFs). The prisms are oriented in such a way so that their axes are parallel to the  $z$ -axis (Fig. 1). Clearly, this orientation permits the correct geometrical modeling of the simulated structure. Each material layer is discretized by making use of several prism layers: one for the silica substrate, two for the gold film, four for the polymer ridge and three for the air above. We note that in Fig. 1 only one prism per material layer is drawn for illustration purposes. The triangular prism element comprises nine edges (detail in Fig. 1), each associated with a respective basis function. Specifically, the basis functions corresponding to the transverse, i.e., belonging to the  $xy$ -plane, edges are given by

$$\mathbf{w}_{ij} = \frac{1}{2} (1 \mp \zeta_0) (\zeta_i \nabla \zeta_j - \zeta_j \nabla \zeta_i), \quad (2)$$

where  $\zeta_i$  and  $\zeta_j$  denote the standard triangle simplex coordinates corresponding to the starting ( $i$ ) and ending ( $j$ ) node of each edge, respectively. The minus sign is used for the basis functions associated with edges of the lower triangular base (edges [1] – [3]), while the plus sign for the ones associated with the upper triangular base (edges [4] – [6]).  $\zeta_0$  is a normalized axial coordinate linearly varying between  $-1$  and  $1$  along the prism axis. For the vertical, i.e., parallel to the  $z$ -axis, edges ([7] – [9]), the basis functions are given by

$$\mathbf{w}_{ij} = \frac{1}{2} \zeta_i \nabla \zeta_0. \quad (3)$$

A more detailed discussion on first- and higher-order prism element basis functions can be found in Refs. Karatzidis and Yioultsis (2008); Graglia et al (1998).

In order to properly truncate the computational domain, absorbing boundary conditions (ABCs) of the first order are implemented on all sides, the top and bottom of the bounding box:

$$\mathbf{n} \times \nabla \times \mathbf{E} + jk_0 \mathbf{n} \times \mathbf{n} \times \mathbf{E} = \mathbf{0}. \quad (4)$$

In addition to that, a perfectly matched layer (PML) with a quadratic profile is employed for the reflectionless termination of the access waveguides [shaded areas in Fig. 2(c)]. The PML is only locally employed, where the absorption requirements are pronounced; its universal utilization would lead to a significant increase of the DoFs and would degrade the conditioning of the finite element matrices. Apart from absorbing reflected modes, the ABC at the input port is also assigned the task of exciting the  $\text{TM}_{00}$  mode. We note that this input-port ABC is slightly modified with respect to the standard ABC with concomitant excitation:

$$\mathbf{n} \times \nabla \times \mathbf{E} + j\beta \mathbf{n} \times \mathbf{n} \times \mathbf{E} = 2j\beta \mathbf{n} \times \mathbf{n} \times \mathbf{E}_{\text{inc}}, \quad (5)$$

in order to account for the coordinate-dependent wave impedance,  $Z_w^{\text{TM}}(x, z)$ , of the  $\text{TM}_{00}$  mode. This is not trivial because the ordinary ABCs are designed for TEM or purely-TM/TE

modes which feature spatially constant wave impedances, while the fundamental mode supported by the DLSPP waveguide is a hybrid one (TM-like). Specifically, the ABC used at the input port reads

$$\mathbf{n} \times \nabla \times \mathbf{E} + j \frac{\omega \mu_0}{Z_w^{\text{TM}}} \mathbf{n} \times \mathbf{n} \times \mathbf{E} = 2j \frac{\omega \mu_0}{Z_w^{\text{TM}}} \mathbf{n} \times \mathbf{n} \times \mathbf{E}_{\text{inc}}, \quad (6)$$

where the wave impedance  $Z_w^{\text{TM}}$  of the TM<sub>00</sub> mode is simply

$$Z_w^{\text{TM}}(x, z) = \frac{E_z(x, z)}{H_x(x, z)}. \quad (7)$$

By comparing Eqs. (5) and (6), one can understand that using the standard input-port ABC would amount to falsely setting the mode wave impedance at a constant value of  $\eta_0/n_{\text{eff}}$ .

Clearly, one must know the distribution of the TM<sub>00</sub> mode field components, in order to be able to implement the input-port ABC. Thus, the first step towards obtaining a solution for the 3D structure is to solve a 2D eigenvalue problem of the waveguide cross-section (ruled rectangle in Fig. 1). This is done again by utilizing the finite element method (Selleri et al 2001), making use of edge elements for the transverse and nodal elements for the axial component. Having solved for the TM<sub>00</sub> mode, we have access to the three components of the magnetic field and the three components of the electric field through differentiation (or vice-versa). Then, it is straight-forward to calculate the mode's spatially-dependent wave impedance  $Z_w^{\text{TM}}$ , defined by Eq. (7). Now that we can implement the input-port ABC, we solve for the E-field in the entire (3D) structure by applying the finite element method to Eq. (1) and imposing the aforementioned boundary conditions. Once the electric field is obtained, the transmission for both output ports, through and drop, is calculated. First, a scalar overlap integral is executed for the dominant electric field component ( $E_z$ ), in order to specify the guided power associated with the TM<sub>00</sub> mode excluding any bend-loss contributions. The overlap integral chosen is of the form

$$\frac{\left| \iint_A E_z(x, z) E_{z,\text{ref}}^*(x, z) dx dz \right|^2}{\iint_A |E_z(x, z)|^2 dx dz \iint_A |E_{z,\text{ref}}(x, z)|^2 dx dz}. \quad (8)$$

The use of a scalar overlap integral is justified by the fact that although the TM<sub>00</sub> mode is hybrid (all field components are non-zero), it is actually quite TM-like, meaning that the dominant electric field component ( $E_z$ ) is an order of magnitude larger than the other transverse component ( $E_x$ ). Hence, the overlap integral of Eq. (8) is a favorable compromise between accuracy and simplicity. Subsequently, we normalize with respect to a reference power level found at the input power port in the absence of the resonator. In the presence of the resonator, the mode propagating in the input waveguide toward the ring is slightly disturbed by bend losses as well as any spurious counter-propagating modes, and hence the additional simulations of the single input waveguide are necessary for a reference power level to be accurately specified. Finally, we should note that the input and output power ports are placed exactly at the boundaries of the resonator [Fig. 2(c)], where the bus waveguides would become accessible in an actual implementation of the filter. Specifically, the input and drop power ports are located at the same y-coordinate and are separated by a distance of  $2R + w$  from the through power port.

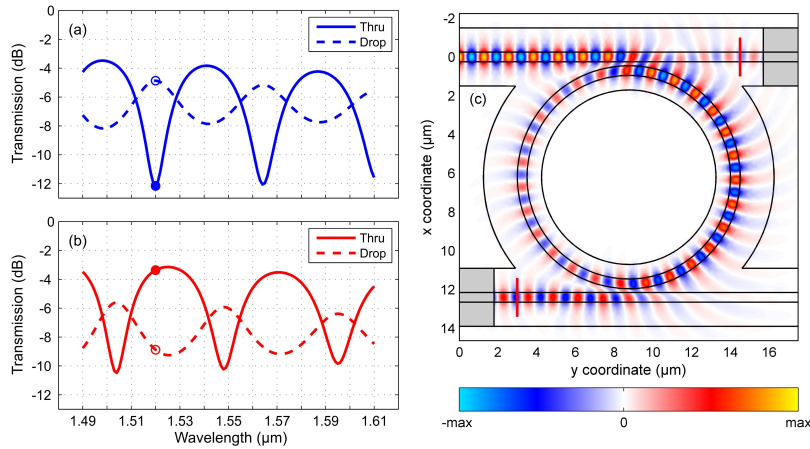


**Fig. 2** Transmission vs. wavelength for both output ports of a microring resonator add-drop filter with  $R = 5.5 \mu\text{m}$  and  $g_1 = g_2 = 0.2 \mu\text{m}$  for (a) the unheated and (b) the heated states. (c) Real part of  $E_z$  at a maximum of the drop port transmission ( $\lambda = 1.52 \mu\text{m}$ ) of the unheated filter. The above maximum is marked in (a) with a hollow blue circle. The  $E_z$  component is plotted at an xy-plane located 10 nm above the metal surface. Shaded areas indicate PML regions and output power ports are marked by red lines.

## 2.2 Results

As an example, let us examine the case of a microring resonator add-drop filter with a radius of  $5.5 \mu\text{m}$ . This radius value is a compromise between competing resistive and bend losses and results in minimal overall losses for the ring resonator. Note that the radius is referring to the fictitious circumference located midway between the inner and outer ring boundaries (Fig. 1). The gaps separating the resonator from the access waveguides are equal, and set to  $0.2 \mu\text{m}$ . Equal gaps ensure the symmetry of the component, meaning that both waveguides are equivalent and that either one can be considered the input waveguide. We also note that the gaps are measured between the edges of resonator and waveguides (Fig. 1). Regarding the gap value chosen, we note that much larger values would not be able to provide the necessary coupling efficiency between input waveguide and resonator. This would translate into shallow transmission dips for the through port and thus poor filter performance. As mentioned in section 1 and evident from Fig. 1, the metallic film is patterned in order to restrict the control current injected in the metallic film for heating purposes. The metallic stripe width is  $3 \mu\text{m}$ . Although such a value is adequate for a straight DLSPP waveguide, a larger value might have been advantageous for the resonator, where the waveguide is bent and the supported mode shifted toward the outside. However, retaining a small width value is crucial to the power consumption of the component. In order to satisfy both demands, the asymmetrical placement of the polymer on the metallic ring is suggested [Fig. 2(c)]. Specifically, with respect to the center of the bent waveguide the metallic ring extends  $1 \mu\text{m}$  toward the inward and  $2 \mu\text{m}$  toward the outward direction.

In Fig. 2 the transmission for both output ports of the microring resonator add-drop filter is depicted. The blue curves [Fig. 2(a)] correspond to the unheated, while the red ones [Fig. 2(b)] to the heated filter ( $\Delta T = 100 \text{ K}$ ). The red curves are shifted toward shorter wavelengths with respect to the blue ones. This is because of the negative thermo-optic coefficient. The aforementioned shift is approximately 16 nm. To illustrate the operation of

the thermally-tunable filter let us now fix the operating wavelength at a maximum of the drop port (e.g. at  $\lambda = 1.52 \mu\text{m}$ ). As is evident from Fig. 2(a), in the absence of heating light exits the drop port with an insertion loss (IL) of  $\sim -4.8 \text{ dB}$ . The through port transmission is smaller by  $\sim 7.4 \text{ dB}$  and therefore crosstalk (XT) is negligible. This can be also seen in Fig. 2(c) where the distribution of the dominant electric field component ( $E_z$ ) is depicted. Clearly, most of the input light couples to the drop port. On the other hand, in the event of heating, light exits the through port [Fig. 2(b)]. In this case, the insertion loss is  $\sim -3.4 \text{ dB}$  and the crosstalk  $\sim -5.5 \text{ dB}$ , respectively. The IL is slightly better and the crosstalk slightly worse compared to the unheated state. Another figure quantifying the filter performance is the extinction ratio (ER) of the output ports. It is found by comparing the transmission levels between different states. Specifically, for the operating wavelength chosen ( $1.52 \mu\text{m}$ ) we find extinction ratios of  $\sim 8.8 \text{ dB}$  and  $\sim 4.1 \text{ dB}$  for the through and drop ports, respectively. Obviously, the drop port ER is quite smaller than that of the through port and rather poor. It is the resonator (roundtrip) losses that limit the drop port ER, and while they affect the through port as well, they are more detrimental to the drop port ER. This is because the drop port transmission, unlike the through port transmission, is not a result of interfering waves. In the case of the through port, such interference effects can be advantageously exploited leading to very small through port transmission minima (critical coupling) and consequently large ERs. On the other hand, the only way of boosting the drop port ER is by increasing the second gap so as to zero out the transmission minima. Although the transmission maxima drop as well, the ratio is improved. Increasing  $g_2$  also permits the through port to further approach critical coupling, since less light couples out of the resonator in the output waveguide. The obvious drawbacks are the larger ILs suffered by the drop port and the fact that the structure becomes asymmetric.

### 3 The beam propagation method in plasmonics

The beam propagation method (BPM) is in its conception a numerical tool used in the study of optical guided-wave structures with small variations along a principal propagation direction or optical axis (Kriezis and Papagiannakis 1997). Exploitation of this feature, in the BPM framework, leads to a key structural reformulation of the vector wave equation, Eq. (1), in the spectral domain: It is converted from its standard elliptic to a parabolic form. As a result, an arbitrary input excitation can be propagated along the optical axis, from one transverse cross-section onto the next, using longitudinal steps of size comparable to the operating wavelength. This stepping algorithm is effectuated with relatively small computational effort, which makes the BPM a suitable tool for the study of optical structures spanning longitudinal dimensions of hundreds of wavelengths.

Despite its widespread application in other areas of integrated photonics (Hoekstra 1997), the BPM has attracted only minor interest in the emerging research field of plasmonics. In fact, except for its use as an eigenmode solver (Shibayama et al 2005; Chen et al 2008), the BPM has not been employed so far in the analysis of any plasmonic component whatsoever. In order to demonstrate its potential applicability in plasmonics as well, we focus on an appropriate example, namely the Mach-Zehnder Interferometric (MZI) switch, implemented on the aforementioned DLSPP waveguiding platform. The MZI switch is depicted in Fig. 3 and comprises, apart from the two parallel arms, two 3 dB couplers to implement the input and output routing of the switch. An optical wave entering the component is divided between the two outputs of the input 3 dB coupler that feed the MZI arms. It can be shown that when the two MZI arms have a zero (or  $\pi$ ) relative phase-shift, the switch is in the CROSS (or

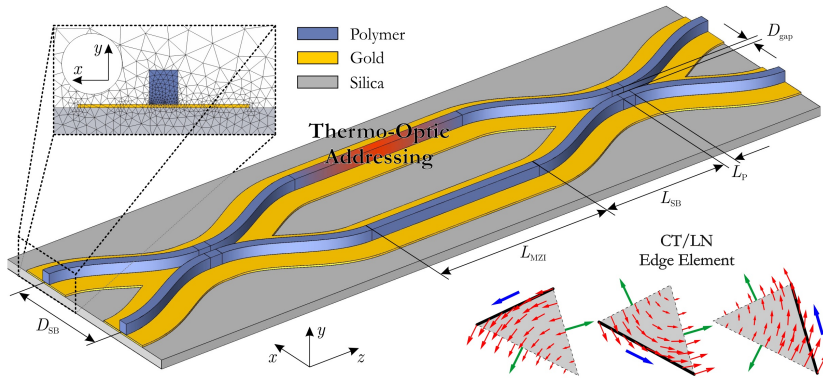


**Fig. 3** Schematic of the DLSPP MZI switch structure with annotation of its principal design parameters. In the upper left corner, a coarse finite element meshing of the transverse cross-section ( $xy$ -plane). In the bottom right corner, the three vector basis-functions of the CT/LN element used for the discretization of the transverse E-field components.

BAR) state, meaning that light recombines on the output port of the output 3 dB coupler that is opposite (or on the same side as) the input port. Switching is effectuated by means of controlling the refractive index of one of the MZI arms, which in turn allows for the control of the phase-shift between the two arms. The refractive index change is induced by the thermo-optic effect, i.e., through heating of the gold-film bearing the thermo-optic polymer ridge of the DLSPP waveguide. By considering the dimensions of the DLSPP-based components that make up the structure (S-bends, couplers, straight sections), along with the available thermo-optic coefficient ( $TOC = -2 \times 10^{-4} \text{ K}^{-1}$  and  $\Delta T = 100 \text{ K}$ ), a device footprint of  $10 \times 100 \mu\text{m}^2$  is estimated. That is about four times larger than the add-drop filter discussed in the previous section. Clearly, this component is too large to be efficiently modeled with any of the numerical methods that directly solve Maxwell's equations. A natural choice for the study of waveguiding structures of this type, i.e. non-reflecting and unidirectional along a longitudinal axis, is the beam propagation method (BPM).

### 3.1 Method implementation details

In this section, we will outline the BPM formulation adopted and highlight only the major implementation considerations particular to the present application. The cumbersome aspects of the analysis will be omitted, referring wherever possible to the relevant literature. Please note that the coordinate-system orientation adopted throughout the present section (Fig. 3) is changed with respect to that used in section 2 (Fig. 1). This means that the dominant electric-field component of the  $\text{TM}_{00}$  mode is now  $E_y$ , instead of  $E_z$ .

The full-vector BPM used in this work employs the finite-element (FE) method for the discretization of the transversal cross-section of the structure, i.e. the  $xy$ -plane in Fig. 3. Triangular first order hybrid finite elements (Koshiba and Tsuji 2000) are used: constant-tangential linear-normal (CT/LN) edge elements for the two transverse components, and conventional nodal elements for the longitudinal component. This amounts to a total of six DoFs per triangular element. The three vector basis functions of the CT/LN element can be seen in the bottom right corner of Fig. 3. The CT/LN elements are fully compatible with the inter-element field continuity conditions, which, as mentioned in section 2, are of major

importance for the proper modeling of plasmonic components or other structures exhibiting similarly dramatic discontinuities in the electromagnetic properties of neighboring materials. It is in part for this reason that the use of finite-difference (FD) schemes for the transverse cross-section was opted out, being problematic at the metal/insulator interfaces. Early efforts undertaken toward the implementation of a FD-BPM were promptly abandoned in favor of the more potent FE-BPM, as the former soon proved inadequate in correctly resolving the propagation losses of the TM<sub>00</sub> mode.

Perfectly matched layers (PML) are used at the cross-sectional boundaries of the computational domain for the reflectionless absorption of radiation expelled from the waveguides. A standard uniaxial PML (Teixeira and Chew 1998) was employed, which demands for the inclusion of diagonal anisotropy in the BPM formulation. The perfectly matched layers are backed with perfect magnetic conductor (PMC) boundary conditions.

We start out by decomposing the vector wave equation, Eq. (1), in two parts, one for the transverse and one for the longitudinal component. We adopt the notation  $[q] \triangleq \bar{\mu}_r^{-1}$  and  $[p] \triangleq \bar{\epsilon}_r$  for the  $3 \times 3$  diagonal anisotropy tensors, and also define the auxiliary transverse  $2 \times 2$  diagonal tensor  $[p'_{tt}] \triangleq \text{diag}\{\epsilon_{yy}, \epsilon_{xx}\}$ .

$$-\frac{\partial^2}{\partial z^2}([p'_{tt}]\mathbf{E}_t) + \frac{\partial}{\partial z}([p'_{tt}]\nabla_t E_z) + \nabla_t \times (p_{zz}\nabla_t \times \mathbf{E}_t) - k_0^2[q_{tt}]\mathbf{E}_t = \mathbf{0}, \quad (9a)$$

$$\frac{\partial}{\partial z}[\nabla_t \cdot ([p'_{tt}]\mathbf{E}_t)] - \nabla_t \cdot ([p'_{tt}]\nabla_t E_z) - k_0^2 q_{zz} E_z = 0. \quad (9b)$$

The decomposition of the wave equation is the necessary first step toward the implementation of the mixed FE discretization discussed earlier. Examination of Eqs. (9) reveals, apart from the coupled nature of the transverse and longitudinal components, that the second-order  $z$ -derivatives are only associated with the transverse component. It has been verified (Schulz et al 1998; Ziogos and Kriegis 2008) that FE-BPM schemes based on this set of equations are numerically unstable. In order to amend this drawback, we adopt the longitudinal field transformation (Schulz et al 1998):

$$E_z \triangleq j \frac{\partial E'_z}{\partial z}. \quad (10)$$

In essence, the transformation of Eq. (10) effectively increases the  $z$ -derivative order associated with the longitudinal field component. After the substitution of Eq. (10), the field envelope is introduced for the transformed field  $\mathbf{E}' = [\mathbf{E}_t, E'_z]^T$ , i.e.  $\mathbf{E}' = \tilde{\mathbf{E}}' e^{-jk_{\text{ref}}z}$ , where tilde denotes the envelope and prime the transformed field. Following standard FEM practice, the Galerkin technique is applied on the resulting equation set. After the assembly of the element contributions of the entire cross-section plane, the 2D-Gauss theorem and the PMC boundary conditions are used to simplify the equation set, which is then recast in matrix form

$$[A] \frac{\partial^2 \tilde{\mathbf{E}}'}{\partial z^2} - j2k_{\text{ref}} [B] \frac{\partial \tilde{\mathbf{E}}'}{\partial z} + [C] \tilde{\mathbf{E}}' = \mathbf{0}, \quad (11)$$

where

$$[A] \triangleq \begin{bmatrix} M_{tt} & -L_{tz} \\ 0 & 0 \end{bmatrix}, \quad [B] \triangleq \begin{bmatrix} M_{tt} & -L_{tz} \\ -\frac{L_{tt}}{2} & -\frac{K_{zz}}{2} \end{bmatrix}, \quad [C] \triangleq \begin{bmatrix} K_{tt} - k_{\text{ref}}^2 M_{tt} & k_{\text{ref}}^2 L_{tz} \\ k_{\text{ref}}^2 L_{zt} & k_{\text{ref}}^2 K_{zz} \end{bmatrix} \quad (12)$$

are the assembled operator-matrices of the propagation equation. The expressions of the constituting submatrices  $M_{tt}$ ,  $L_{zt}$ ,  $L_{tz}$ ,  $K_{tt}$  and  $K_{zz}$  can be found in Saitoh and Koshiba (2001). We have verified that a paraxial FE-BPM scheme based on Eqs. (11)-(12) is, almost in all

cases, unstable. This is not altogether unexpected, noting that the second-order  $z$ -derivatives are only present in the first equation, i.e. the one stemming from the transverse part. In order to counteract this drawback, the FE-BPM equation-set can be cast in a slightly different arrangement (Schulz et al 1998; Saitoh and Koshiba 2001). More specifically, the operator-matrices associated with the first and second  $z$ -derivatives in Eq. (11) satisfy the relation

$$[B] \equiv [A] = [A'] \triangleq \begin{bmatrix} M_{tt} & -L_{tz} \\ -L_{zt} & -K_{zz} \end{bmatrix}. \quad (13)$$

This reformulation permits stable propagation by conveniently allowing for the introduction of the wide-angle (WA) approximation (Hadley 1992b), thus avoiding the limitations of any paraxial approximation. The modification implied, as we understand it, is related to the second row of matrix equations (11)-(12), i.e., the equation of the longitudinal field component. For the DLSPP waveguide, the longitudinal component is weaker than the dominant transverse component. In the BPM framework, this means that the aggregate effect on stability and accuracy of any perturbation on the longitudinal component is expected to be minor. However, caution has to be taken when dealing with longitudinally varying structures where the approximations used in the BPM are put to more stringent testing.

As discussed in the previous paragraph, the introduction of Eq. (13) into Eq. (11) permits the iterative approximation of the propagator implied therein, by means of the recurrence relation (Hadley 1992b)

$$\frac{\partial}{\partial z} \Big|_n \tilde{\mathbf{E}}' = \frac{-\hat{P}}{\frac{\partial}{\partial z} \Big|_{n-1} - 2jk_{\text{ref}}} \tilde{\mathbf{E}}', \quad (14)$$

where  $(\partial/\partial z)_{n=0} \equiv 0$  and  $\hat{P} \triangleq [A']^{-1}[C]$ . For a given iteration order ( $n$ ), the RHS of Eq. (14) corresponds to a rational Padé( $r,s$ ) polynomial approximation of the Helmholtz operator of Eq. (11). According to Hadley (1992a), performing a high number of iterations ( $n = r + s$ ) on Eq. (14) produces a propagator with high order Padé polynomials of operator  $\hat{P}$  in the RHS of Eq. (14).

Rewriting the propagation equation, Eq. (14), using operator notation

$$\frac{\partial}{\partial z} \tilde{\mathbf{E}}' = \left( \frac{\hat{N}}{\hat{D}} \right)_n \tilde{\mathbf{E}}', \quad (15)$$

implies that the resulting propagator, i.e. the RHS of Eqs. (14)-(15), is a function of the WA approximation order used ( $n$ ), the assembled operator-matrices ( $[A']$ ,  $[C]$ ), and the reference wavevector ( $k_{\text{ref}}$ ). A finite difference approximation is utilized in the propagation direction, i.e. for the LHS of Eq. (15), in conjunction with the Crank-Nicolson (CN) scheme for the RHS of Eq. (15), to ensure control over numerical stability. The BPM equations are thus recast in their final form:

$$[\hat{D} + j(1 - a_{\text{CN}})\Delta z \hat{N}] \tilde{\mathbf{E}}'(z_0 + \Delta z) = [\hat{D} - ja_{\text{CN}}\Delta z \hat{N}] \tilde{\mathbf{E}}'(z_0), \quad (16)$$

where  $a_{\text{CN}} \in (0.5, 1]$  is the parameter controlling the stability of the scheme. The operators  $\hat{N}$  and  $\hat{D}$  are polynomials of operator  $\hat{P}$ , the order of each depending on the WA approximation order ( $n$ ) used. Factorizing the resulting polynomials of  $\hat{P}$ , on each side of Eq. (16), and utilizing the grouped nominator and denominator roots sequentially in a multi-step algorithm, allows for the higher order WA approximations to be implemented in the BPM. Iteration order  $n = 1$  leads to a Padé(1,0) approximation and corresponds to a paraxial BPM. The WA-BPM presented in Saitoh and Koshiba (2001); Schulz et al (1998) corresponds to  $n = 2$ ,

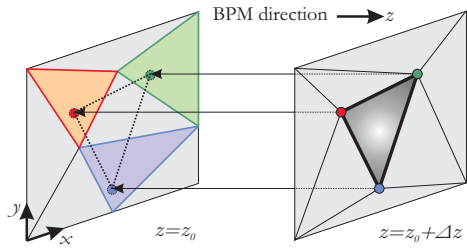


**Fig. 4** The DoFs interpolation procedure for longitudinally varying guided-wave structures. For simplicity's sake, only the nodal DoF interpolation is depicted. The vector (edge) DoFs are similarly interpolated with respect to the element edge midpoints.

i.e., Padé(1, 1). Numerical solution of the sparse equation systems described by Eq. (16), permits the iterative computation of the propagated field at the “next  $z$ -step” ( $z = z_0 + \Delta z$ ), given an input field at the “current  $z$ -step” ( $z = z_0$ ) and the operators  $\hat{N}$ ,  $\hat{D}$ . These depend on the waveguide cross-section ( $\hat{P}$ ), the reference wavevector ( $k_{\text{ref}}$ ) and the WA approximation order ( $n$ ) used.

Having introduced the basic concepts of the appropriately adapted FE-BPM for the study of plasmonic components, we will now proceed with the discussion of some important implementation issues concerning longitudinally varying structures, like the MZI switch we analyze in the next subsection.

The BPM simulation of longitudinally varying structures inevitably introduces a staircasing approximation along the propagation axis ( $z$ ), as it requires the re-generation of the FE mesh after each propagation step, regardless of the  $z$ -step size, in order to accurately describe each “next-step” cross-section. Finite element assembly is then performed on the new mesh. Consequently, the projection of the DoFs associated with the previous mesh onto the new one is required, so as to use the field they describe as an excitation input for the present  $z$ -step. This procedure increases the computational overhead and inevitably introduces approximation errors due to the interpolation illustrated in Fig. 4. Nevertheless, in conjunction with the WA scheme, the mesh-regeneration was found to effectively minimize the off-axis-propagation and staircasing approximation error of the BPM.

In the present work, WA approximations up to Padé(4, 4) were tested and were found to considerably increase the method accuracy at the obvious expense of computation-time. In principle, a multistep Padé(4, 4) scheme would require four times the CPU-time of a single-step Padé(1, 1) scheme. However, for longitudinally varying structures, we recorded only twice longer execution time. This is attributed to the principal effect of another bottleneck, namely the inevitable computational overhead associated with FE-mesh regeneration at each step.

Furthermore, the operators of the RHS and the LHS of Eq. (16) can be associated with the electromagnetic properties of the “next” or the “current”  $z$ -step cross-section. However, for the DLSPP waveguides studied in this work, our investigations showed that both propagators should be associated with the same  $z$ -step cross-section to ensure stable propagation. Whichever was the choice, i.e., the association with a cross-section, we stress that both these operators are necessarily defined on the same FE-mesh, for obvious implementation reasons.

As a final remark, it should be noted that, in the framework of the WA-BPM, the power-conservation and phase-accuracy demands are difficult to meet simultaneously (Deng and Yevick 2005), even more for longitudinally varying structures. Increasing the phase-accuracy, e.g. by employing higher-order WA-schemes, high values of the CN-parameter or small  $z$ -steps, inevitably downgrades the power-conservation, and vice-versa. So, in the study of the MZI to follow, we appropriately chose the BPM parameters in a case-sensitive approach. For the design of the 3 dB couplers and the calculation of the output-port extinction

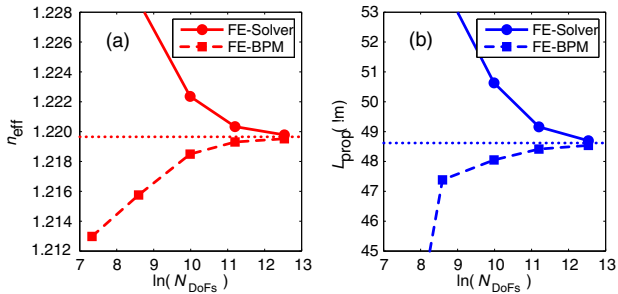


**Fig. 5** Convergence of (a) the effective index,  $n_{\text{eff}}$ , and (b) the propagation length,  $L_{\text{prop}}$ , with increasing FE-mesh resolution,  $N_{\text{DoFs}}$ . Comparison of the FE-BPM used in this work with a standard FE-based solver with identical FE-mesh. The horizontal dotted lines represent the approximate converged values.

tion, both being phase-sensitive studies, high-accuracy parameters were used: WA-Padé(4,4),  $a_{\text{CN}} \geq 0.60$  and  $\Delta z \approx 0.125 - 0.250 \mu\text{m}$ . For power-related applications, i.e. the estimation of the total insertion losses, parameters for better power-conservation were chosen: WA-Padé(1,1),  $a_{\text{CN}} \leq 0.51$  and  $\Delta z \approx 0.250 - 0.500 \mu\text{m}$ . Regarding single-mode waveguide BPM simulations, the reference refractive index of the method ( $n_{\text{ref}}$ ) should in all cases be set equal to the real part of the effective propagation index ( $n_{\text{eff}}$ ) of the fundamental mode for the given FE-mesh, in order to minimize numerical dissipation.

### 3.2 Results

In this section, we outline the modeling procedure for the MZI switch using the full-vector FE-BPM described in the previous section.

Firstly, the BPM is used as an eigenmode solver (Saitoh and Koshiba 2001), in order to calculate the E-field component profiles and the effective index of the fundamental DLSPP mode. In the study of the MZI switch that will follow, these will serve as input-excitation and reference-index, respectively. The waveguide studied is defined in section 1 and the operating wavelength is  $\lambda_0 = 1.55 \mu\text{m}$ . The fundamental mode is found to converge relatively fast along real-distance propagation. Note that the imaginary distance propagation procedure is inapplicable for the DLSPP waveguide, since it favors the SPP-mode supported on the gold/silica interface as its effective propagation index is higher than that of the TM<sub>00</sub> mode. The convergence of the calculated effective index  $n_{\text{eff}}$  and propagation length ( $L_{\text{prop}}$ ), with respect to the FE-mesh resolution ( $N_{\text{DoFs}}$ ), is compared to that obtained by means of a FE-based eigenmode solver (Selleri et al 2001) using identical meshes, Fig. 5. It is evident that the BPM converges to the same values as the solver, somewhat faster than the latter and from an opposite direction. The calculated propagation constant at  $N_{\text{DoFs}} \approx 270,000$  corresponds to an effective index of  $n_{\text{eff}} \approx 1.2195$  and a propagation length of  $L_{\text{prop}} \approx 48.5 \mu\text{m}$ .

The following step in the study of the MZI switch is the design of the (identical) input/output 3 dB couplers for the reference design wavelength ( $\lambda_0$ ). This task consists of carefully setting the associated structural parameters  $L_{\text{SB}}$ ,  $L_{\text{P}}$ ,  $D_{\text{SB}}$ ,  $D_{\text{gap}}$  depicted in Fig. 3. The dimensions of the S-bends, i.e. the length ( $L_{\text{SB}}$ ) and the lateral displacement [ $(D_{\text{SB}} - D_{\text{gap}})/2$ ], can be chosen so as to attain an aggregate minimum of the bend and propagation losses (Krasavin and Zayats 2008). The respective values adopted in this work are  $L_{\text{SB}} = 10 \mu\text{m}$  and  $D_{\text{SB}} = 6 \mu\text{m}$ . Having set these dimensions, the necessary length of the parallel-running polymer ridges between the S-bends ( $L_{\text{P}}$ ) needed to achieve 3 dB coupling is a function of the gap between the two polymer guiding ridges ( $D_{\text{gap}}$ ). This has been numerically calculated using the full-vector FE-BPM in the following manner: The fundamental mode is launched in one input port of the 3 dB coupler and it is propagated up to

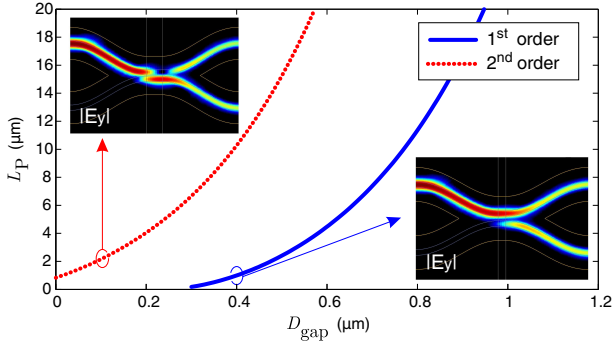


**Fig. 6** Design of the 3 dB couplers used for the input/output routing of the MZI  $2 \times 2$  switch. The polymer gap ( $D_{\text{gap}}$ ) and the parallel-running length ( $L_P$ ) are defined in the schematic presented in Fig. 3, and  $L_{\text{SB}} = 10 \mu\text{m}$  and  $D_{\text{SB}} = 6 \mu\text{m}$ . The FE-BPM used was based on a WA Padé(4,4) scheme, the Crank-Nicolson parameter was  $a_{\text{CN}} = 0.60$  and the longitudinal step was  $\Delta z = 0.125 \mu\text{m}$ .

its output ports, where the guided power in each arm is measured. An output-port extinction ratio of 0 dB signifies an ideal 50/50 coupler. The results are presented in Fig. 6, where it can be seen that for small gaps ( $D_{\text{gap}} < 300 \text{ nm}$ ) second-order coupling is employed in order to achieve 3 dB coupling. The reason is that, since the coupling for small gaps is so strong, light passes entirely onto the opposite guide and is then equally split between the output ports. Second-order 3 dB-coupling leads to longer structures, something to be avoided in plasmonic components due to the inherent losses, thus setting a minimum to the polymer gap choice. It is stressed that the results of Fig. 6 are only valid for the S-bend parameters defined above, since, as witnessed from the insets, the inner parts of the S-bends also contribute significantly to the coupling. For the remainder of this paragraph a  $D_{\text{gap}} = 400 \text{ nm}$  gap is chosen that corresponds to  $L_P \approx 900 \text{ nm}$ . This ensures that the fabrication-related resolution requirements are minimal and can be met with most available lithographic techniques, while the component length is restricted to the lowest possible value. For these dimensions, the total insertion losses of the 3 dB-couplers are estimated with the FE-BPM to be below 3 dB, accounting for both propagation and bend losses.

In order to assess the necessary MZI arm length for a  $\pi$ -phase-shift, the FE-BPM was used once more as an eigenmode solver: we calculated the effective propagation index when the thermo-optic polymer ridge is heated ( $\Delta n = \Delta T \times \text{TOC} = -2 \times 10^{-2}$ ), and compared this value to that of the unheated state. It can be shown that the necessary length for the MZI arms is given by:  $L_\pi = 0.5\lambda_0 / \Delta n_{\text{eff}}^{\text{Cool-Hot}}$ . The arm length was found to be  $L_{\text{MZI}} \approx 47.6 \mu\text{m}$ .

Finally, the entire MZI structure was simulated for both states (BAR, CROSS) to assess the overall performance. The resulting evolutions of the dominant E-field component ( $E_y$ ) along the MZI are displayed in Fig. 7. We note that the BPM simulation of the DLSPP structure produces very smooth field evolutions with almost no evidence of numerical nuisances. Commenting on the particular MZI switch, the minimum simulated output port extinction was  $ER_{\min} = 29 \text{ dB}$ . The insertion losses were approximately 11 dB, a value consistent with the total propagation distance ( $< 90 \mu\text{m}$ ), the nominal propagation losses ( $< 0.1 \text{ dB}/\mu\text{m}$ ) and the standard bend-losses associated with the S-bends ( $< 0.5 \text{ dB}$  per bend).

#### 4 Summary and conclusions

This work demonstrates the application potential of two widely acclaimed numerical methods, namely the finite element and the beam propagation method, in the emerging research area of plasmonics. The formulation of the two methods is outlined, carefully adapted for the particular application environment, and supported by a discussion of the principal imple-

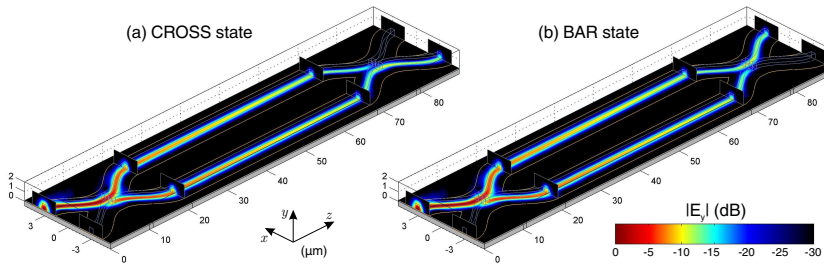


**Fig. 7** Evolution of the dominant E-field component ( $E_y$ ) intensity in dB, for the two switch states, (a) CROSS, when both arms are unheated, and (b) BAR, when one arm is heated. The FE-BPM used was based on the WA-Padé(4,4) scheme for the longitudinally-varying sections and the WA-Padé(1,1) scheme for the straight sections. The Crank-Nicolson parameter was  $a_{CN} = 0.505$  and the longitudinal step was  $\Delta z = 0.125 \mu\text{m}$  and  $\Delta z = 0.250 \mu\text{m}$  for the longitudinally-varying and the straight sections, respectively.

mentation aspects. In order to evaluate the methods' performance, two typical DLSPP-based plasmonic components are studied. More specifically, a microring resonator add-drop filter and a Mach-Zehnder interferometric switch are analyzed with the finite element method and the beam propagation method, respectively. The obtained results clearly show that both methods can accurately model light propagation in plasmonic components.

**Acknowledgements** This work was supported by the European FP7 project PLATON [Contract No. 249135], the Greek State Scholarships Foundation (IKY), and the "Alexander S. Onassis" public benefit foundation.

## References

- Chen J, Li Z, Fan Z, Yang F (2008) Finite element beam propagation method for analysis of plasmonic waveguide. *Chin Opt Lett* 6(8):572–574
- Deng H, Yevick D (2005) The nonunitarity of finite-element beam propagation algorithms. *IEEE Photon Technol Lett* 17(7):1429–1431
- Ebbesen TW, Genet C, Bozhevolnyi SI (2008) Surface-plasmon circuitry. *Phys Today* 61:44–50
- Gosciniak J, Bozhevolnyi SI, Andersen TB, Volkov VS, Kjelstrup-Hansen J, Markey L, Dereux A (2010) Thermo-optic control of dielectric-loaded plasmonic waveguide components. *Opt Express* 18(2):1207–1216
- Graglia RD, Wilton DR, Peterson AF, Gheorma I-L (1998) Higher order interpolatory vector bases on prism elements. *IEEE Trans Antennas and Propag* 46(3):442–450
- Gramotnev DK, Bozhevolnyi SI (2010) Plasmonics beyond the diffraction limit. *Nat Photonics* 4(2):83–91
- Grandidier J, Colas des Francs G, Markey L, Bouhelier A, Massenot S, Weeber J-C, Dereux A (2010) Dielectric-loaded surface plasmon polariton waveguides on a finite-width metal strip. *Appl Phys Lett* 96(6):063,105
- Hadley GR (1992a) Multistep method for wide-angle beam propagation. *Opt Lett* 17(24):1743–1745
- Hadley GR (1992b) Wide-angle beam propagation using Padé approximant operators. *Opt Lett* 17(20):1426–1428
- Hoekstra HJWM (1997) On beam propagation methods for modelling in integrated optics. *Opt Quant Electron* 29(2):157–171
- Holmgård T, Bozhevolnyi SI (2007) Theoretical analysis of dielectric-loaded surface plasmon-polariton waveguides. *Phys Rev B* 75:245,405
- Holmgård T, Chen Z, Bozhevolnyi SI, Markey L, Dereux A (2009a) Dielectric-loaded plasmonic waveguide-ring resonators. *Opt Express* 17(4):2968–2975
- Holmgård T, Chen Z, Bozhevolnyi SI, Markey L, Dereux A, Krasavin AV, Zayats AV (2009b) Wavelength selection by dielectric-loaded plasmonic components. *Appl Phys Lett* 94:051,111
- Jin J (2002) The Finite Element Method in Electromagnetics, 2nd edn. John Wiley & Sons, New York
- Karatzidis DI, Yioultsis TV (2008) Efficient analysis of planar microwave circuits with mixed-order prism vector finite macroelements. *Int J Numer Model* 21(6):475–492

- Koshiba M, Tsuji Y (2000) Curvilinear hybrid edge/nodal elements with triangular shape for guided-wave problems. *J Lightwave Technol* 18(5):737–743
- Krasavin AV, Zayats AV (2008) Three-dimensional numerical modeling of photonic integration with dielectric-loaded SPP waveguides. *Phys Rev B* 78:045,425
- Kriezis EE, Papagiannakis AG (1997) A three-dimensional full vectorial beam propagation method for z-dependent structures. *IEEE J Quant Electron* 33(5):883–890
- Palik ED (ed) (1985) *Handbook of Optical Constants of Solids*, 1st edn. Academic Press, New York
- Raether H (1988) *Surface Plasmons on Smooth and Rough Surfaces and on Gratings*. Springer-Verlag, Berlin
- Saitoh K, Koshiba M (2001) Full-vectorial finite element beam propagation method with perfectly matched layers for anisotropic optical waveguides. *J Lightwave Technol* 19(3):405–413
- Schulz D, Glingener C, Bludszuweit M, Voges E (1998) Mixed finite element beam propagation method. *J Lightwave Technol* 16(7):1336–1341
- Selleri S, Vincetti L, Cucinotta A, Zoboli M (2001) Complex FEM modal solver of optical waveguides with pml boundary conditions. *Opt Quant Electron* 33:359–371
- Shibayama J, Yamazaki T, Yamauchi J, Nakano H (2005) Eigenmode analysis of a light-guiding metal line loaded on a dielectric substrate using the imaginary-distance beam-propagation method. *J Lightwave Technol* 23(3):1533–1539
- Teixeira FL, Chew WC (1998) General closed-form PML constitutive tensors to match arbitrary bianisotropic and dispersive linear media. *IEEE Microwave and Guided Wave Lett* 8(6):223–225
- Tsilipakos O, Kriezis EE (2010) Microdisk resonator filters made of dielectric-loaded plasmonic waveguides. *Opt Commun* 283(15):3095–3098
- Tsilipakos O, Yioultsis TV, Kriezis EE (2009) Theoretical analysis of thermally tunable microring resonator filters made of dielectric-loaded plasmonic waveguides. *J Appl Phys* 106(9):093,109
- Wu M, Han Z, Van V (2010) Conductor-gap-silicon plasmonic waveguides and passive components at sub-wavelength scale. *Opt Express* 18(11):11,728–11,736
- Yu Z, Veronis G, Fan S, Brongersma ML (2008) Gain-induced switching in metal-dielectric-metal plasmonic waveguides. *Appl Phys Lett* 92(4):041,117
- Ziogos GD, Kriezis EE (2008) Modeling light propagation in liquid crystal devices with a 3-D full-vector finite-element beam propagation method. *Opt Quant Electron* 40(10):733–748